



# A mixed total Lagrangian-updated Lagrangian Smoothed Particles Hydrodynamics method for geomechanics simulations with discontinuities

Daniel S. Morikawa<sup>1</sup>, Mitsuteru Asai<sup>2</sup>

<sup>1</sup>*Center for Mathematical Science and Advanced Technology (MAT), JAMSTEC  
3173-25, Showa-machi, Kanazawa-ku, Yokohama, Kanagawa, 236-0001, JAPAN  
morikawad@jamstec.go.jp*

<sup>2</sup>*Department of Civil and Structural Engineering, Kyushu University  
744 Motoooka, Nishi Ward, Fukuoka, 819-0395, JAPAN  
asai@doc.kyushu-u.ac.jp*

**Abstract.** This study presents a novel approach for simulating geotechnical problems including the initiation and post-failure behavior of discontinuities. The developed method is constituted by a mixed total Lagrangian–updated Lagrangian Smoothed Particle Hydrodynamics (SPH) method, which the main characteristic is to distinguish between internal forces within a body, represented by the internal stress, from contact forces interactions with other bodies, as collision stress. Internal stress effects are calculated using total Lagrangian SPH interpolations, while collision stress effects are computed with updated Lagrangian. discontinuities are simulated by employing plastic deformation as a damage measure, in which fully damaged particles detached from their original body are treated as a separate particulate material with neighboring interactions via collision stress.

**Keywords:** Landslide, Smoothed particle hydrodynamics, Total Lagrangian, Discontinuities, Discontinuities

## 1 Introduction

Smoothed Particle Hydrodynamics (SPH) has emerged as a numerical method for simulating astrophysical problems [1, 2], and it was soon acknowledged as a versatile method by being used in various applications including fluid dynamics (e.g., Monaghan [3], Asai et al. [4], Morikawa et al. [5, 6]), fluid-structure interaction (FSI) (e.g. Khayyer et al. [7], Morikawa and Asai [8]) and solid mechanics (e.g. Bonet and Lok [9], Lee et al. [10, 11]), to name a few. Unlike grid-based methods, SPH represents the materials with discrete Lagrangian particles, allowing for efficient and accurate modeling of large deformations.

Under this premise, several researchers have used the SPH method for landslide simulations such as Bui et al. [12], Blanc and Pastor [13], Morikawa and Asai [14, 15] and others. However, the appearance of discontinuities within the soil mass as the landslide mass detaches is still a great challenge. The primary objective of this study is to introduce a novel SPH method capable of simulating the post-failure behavior of detached soil masses including self-contact interactions. By integrating the stability and accuracy of the total Lagrangian framework with the adaptability of the updated Lagrangian, our method aims to accurately represents the complex interactions between intact and detached regions within a soil mass during landslide events. All the codes are authorial and run in a single GPU with a NVIDIA A100 graphic card.

## 2 The SPH Method

The SPH method is a Lagrangian meshless particle method in which functions are approximated according to a weighted summation of the interactions with neighboring particles [1, 2]. In most of SPH applications, the most relevant SPH operators are the spatial derivatives. In the current work, we use a corrected version developed by Bonet and Lok [9], Randles and Libersky [16], Ganzenmüller [17] that improves the accuracy of the first derivative evaluation. Such equations are shown in details in the next subsection, and all of them use the concept of corrected kernel gradient  $\tilde{\nabla}W_{ij}$  which is defined as

$$\tilde{\nabla}W_{ij} = \left( \sum_j \frac{m_j}{\rho_j} \nabla W_{ij} \otimes \mathbf{r}_{ji} \right)^{-1} \nabla W_{ij}; \quad \tilde{\nabla}_0 W_{ij} = \left( \sum_j \frac{m_j}{\rho_j} \nabla_0 W_{ij} \otimes \mathbf{R}_{ji} \right)^{-1} \nabla_0 W_{ij}, \quad (1)$$

in the updated and total Lagrangian frameworks, respectively. In the above equations,  $i$  and  $j$  stands for a target and a neighbor particle, respectively,  $m$  the mass,  $\rho$  the density,  $\mathbf{r}_{ij} = \mathbf{x}_i - \mathbf{x}_j$  the relative position vector in the current configuration,  $\mathbf{R}_{ij} = \mathbf{X}_i - \mathbf{X}_j$  the relative position vector in the reference configuration and  $W$  the weight function (also called kernel). In this study, we selected the cubic spline kernel [18] with reduced influence radius  $h_{\text{inf}}$  of  $1.99d$ , where  $d$  is the particle diameter. Using the cubic spline kernel, the smoothing length can be defined as  $h = h_{\text{inf}}/2$ .

## 2.1 Neighboring search in the mixed updated Lagrangian-total Lagrangian framework

Let us consider a target particle  $i$ . In this study, we define the group of neighboring particles under the influence of the internal and collision stress, respectively, as

$$\mathbb{T}_i \equiv \{j = 1, 2, \dots, N \mid R_{ij} < h_{\text{inf}} \wedge \mathbf{x}_j \in \Omega_i \wedge D_i, D_j < 1\}, \quad (2)$$

$$\mathbb{U}_i \equiv \{j = 1, 2, \dots, N \mid r_{ij} < h_{\text{inf}} \wedge (\mathbf{x}_j \notin \Omega_i \vee D_i = 1 \vee D_j = 1 \vee R_{ij} > 2h_{\text{inf}})\}. \quad (3)$$

In summary, neighboring particles that share the same body ( $\Omega$ ) and are not fully damaged ( $D < 1$ ) are contained in  $\mathbb{T}$ , that is, their neighboring search are conducted in the total Lagrangian framework. On the other hand, neighboring particles from different bodies or in contact after a discontinuity are contained in  $\mathbb{U}$ , that is, with neighbors in updated Lagrangian. Another specificity of the current method is that we consider a smaller influence radius than usual to avoid the influence of particles far apart ( $h_{\text{inf}} = 1.99d$ ).

With the above definitions, it is now possible to define corrected gradient operators in both updated and total Lagrangian frameworks as

$$\langle \nabla f \rangle_i = \sum_{j \in \mathbb{T}_i} \frac{m_j}{\rho_j} (f_j - f_i) \tilde{\nabla}W_{ij}; \quad \langle \nabla_0 f \rangle_i = \sum_{j \in \mathbb{U}_i} \frac{m_j}{\rho_j} (f_j - f_i) \tilde{\nabla}_0 W_{ij} \quad (4)$$

$$\tilde{\nabla}W_{ij} = \mathbf{L}_i \nabla W_{ij}; \quad \tilde{\nabla}_0 W_{ij} = \mathbf{L}_i \nabla_0 W_{ij}; \quad \mathbf{L}_i = \left( \sum_{j \in \mathbb{T}_i} \frac{m_j}{\rho_j} \nabla_0 W_{ij} \otimes \mathbf{R}_{ji} + \sum_{j \in \mathbb{U}_i} \frac{m_j}{\rho_j} \nabla W_{ij} \otimes \mathbf{r}_{ji} \right)^{-1}. \quad (5)$$

## 3 Formulation

Let us formulate the governing equations using the premises of continuum mechanics. A body may be subjected to volumetric forces  $\mathbf{b}$  and *surface forces*  $\mathbf{t}$ . Such surface forces may be divided into *internal forces* resulting from interactions between adjacent body parts represented by a traction vector  $\mathbf{t}_i$  (or  $\mathbf{T}_i$ ) and *contact forces* as a result of interactions with outer bodies represented by  $\mathbf{t}_c$  (or  $\mathbf{T}_c$ ) at  $\Gamma_c$ , so that  $\mathbf{t} = \mathbf{t}_i + \mathbf{t}_c$ . Following Cauchy's Theorem, the body forces of the material may be represented by a second order vector called Cauchy stress  $\boldsymbol{\sigma}$  or nominal stress  $\mathbf{P}$  such that  $\mathbf{t} = \boldsymbol{\sigma} \cdot \mathbf{n}$  (or  $\mathbf{T} = \mathbf{P} \cdot \mathbf{n}_0$ , in the reference configuration), where  $\mathbf{n}$  is the normal direction vector. Applying the Cauchy's Theorem for the contact forces, we define the *contact stress*  $\boldsymbol{\sigma}_c$  as  $\mathbf{t}_c = \boldsymbol{\sigma}_c \cdot \mathbf{n}$ .

The concept of contact stress has been first described by Hertz in 1882 [19, 20], and it is one of the key concepts for the field of contact mechanics. We do not define the nominal stress for the contact forces because we do not use it in our proposed method. In addition, we denote the stress tensor for the internal forces  $\mathbf{t}_i$  simply as  $\boldsymbol{\sigma}$  (or  $\mathbf{P}$ ), for simplification.

### 3.1 Governing equations

Applying the conservation of linear momentum to a body subjected to all conditions described previously and decomposing the traction vector as  $\mathbf{t} = \mathbf{t}_i + \mathbf{t}_c$ , using the Gauss's Theorem, we derive

$$\frac{D\mathbf{v}}{Dt} = \frac{1}{\rho} \nabla \cdot \boldsymbol{\sigma} + \frac{1}{\rho} \nabla \cdot \boldsymbol{\sigma}_c \Big|_{\Gamma_c} + \mathbf{b}, \quad (6)$$

where  $D/Dt$  is the time derivative and  $\mathbf{v}$ , the velocity. In addition, the evolution of the deformation gradient  $\mathbf{F} = \partial \mathbf{x} / \partial \mathbf{X}$  can be defined as [21]

$$\frac{D\mathbf{F}}{Dt} = (\nabla_0 \otimes \mathbf{v})^T. \quad (7)$$

In the current work, we use the total Lagrangian form, i.e., the reference configuration, to calculate the acceleration caused by  $\boldsymbol{\sigma}$ , while using the updated Lagrangian form, i.e., the current configuration, for  $\boldsymbol{\sigma}_c$ . Also, we decided to use  $\rho_0$  instead of  $\rho$ , since it is a prescribed value that does not evolve with time. Therefore, we may rewrite Eq. (6) by transforming  $\boldsymbol{\sigma}$  into  $\mathbf{P}$  and  $\boldsymbol{\sigma}_c$  into  $\boldsymbol{\tau}_c$  as

$$\frac{D\mathbf{v}}{Dt} = \frac{1}{\rho_0} \nabla_0 \cdot \mathbf{P} + \frac{1}{\rho_0} \nabla \cdot \boldsymbol{\tau}_c \Big|_{\Gamma_c} + \mathbf{b}, \quad (8)$$

where  $\boldsymbol{\tau}$  is the Kirchoff stress. To simplify the notation, we will denote  $\nabla \cdot \boldsymbol{\tau}_c \Big|_{\Gamma_c}$  by simply  $\nabla \cdot \boldsymbol{\tau}_c$  from now on. Finally, Eqs. (8) and (7) can be discretized in time using a symplectic time integration scheme as

$$\mathbf{v}^{n+1} = \mathbf{v}^n + \Delta t \left( \frac{1}{\rho_0} \nabla_0 \cdot \mathbf{P} + \frac{1}{\rho_0} \nabla \cdot \boldsymbol{\tau}_c + \mathbf{b} \right), \quad (9)$$

$$\mathbf{F}^{n+1} = \mathbf{F}^n + \Delta t (\nabla_0 \otimes \mathbf{v})^T, \quad (10)$$

where the superscripts  $n$  and  $n + 1$  refer to previous and next time steps, respectively.

## 4 Finite strain elastoplasticity

The current method is based on finite strain elastoplasticity, which is more suitable for large deformation problems. The formulation described below is similar to the one presented in [8, 15]. We use the Hencky model to calculate the elastic part of the stress, which makes it convenient to adapt to any type of yield criteria for the plastic part. The stress (in this case, the Kirchoff stress) has a linear relationship with the logarithmic strain as

$$\boldsymbol{\tau} = \mathbf{C}_{el} : \boldsymbol{\epsilon}; \quad \boldsymbol{\epsilon} = \frac{1}{2} \ln \mathbf{B}, \quad (11)$$

where  $\mathbf{C}_{el}$  is the tangent modulus for the Hookean material,  $\boldsymbol{\epsilon}$  is the logarithmic strain, and  $\mathbf{B} = \mathbf{F} \cdot \mathbf{F}^T$  is the left Cauchy-Green strain tensor. Notice that the symbol  $\ln$  refers to the tensor logarithmic operation, which is different from the scalar logarithmic operator  $\ln$ .

### 4.1 Internal stress return mapping

The current method is based on the multiplicative split between elastic and plastic deformation gradients ( $\mathbf{F} = \mathbf{F}_e \cdot \mathbf{F}_p$ ). Using the logarithmic strain and some logarithm properties, it is straightforward to derive  $\boldsymbol{\epsilon} = \boldsymbol{\epsilon}_e + \boldsymbol{\epsilon}_p$ . In this way, using the Hencky model and a conventional return mapping algorithm, we update the stress as

$$\boldsymbol{\tau}^{n+1} = \boldsymbol{\tau}^{\text{trial}} - \Delta \gamma \mathbf{C}_{el} : \mathbf{N}^{n+1}, \quad (12)$$

$$\mathbf{B}^{\text{trial}} = \Delta \mathbf{F} \cdot \mathbf{B}^n \cdot \Delta \mathbf{F}, \quad \Delta \mathbf{F} = \mathbf{I} + \Delta t (\nabla_0 \otimes \mathbf{v})^T \cdot (\mathbf{F}^n)^{-1}, \quad (13)$$

$$\boldsymbol{\epsilon}^{\text{trial}} = \frac{1}{2} \ln \mathbf{B}^{\text{trial}}, \quad \boldsymbol{\tau}^{\text{trial}} = \mathbf{C}_{el} : \boldsymbol{\epsilon}^{\text{trial}}. \quad (14)$$

where  $\Delta \gamma$  is the plastic multiplier,  $\mathbf{N}$  is the direction of the plastic flow, and the superscript “trial” refers to a trial state of the stress.

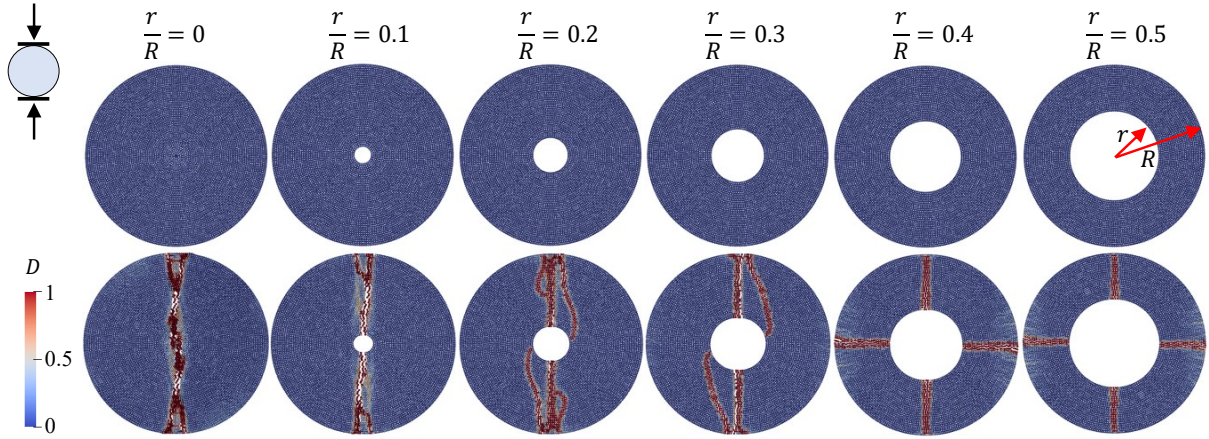


Figure 1. Brazilian test: snapshot of simulation results for different values of  $r/R$  at  $\varepsilon = 0$  and  $\varepsilon = 0.1\%$

## 4.2 Collision stress return mapping and discontinuity initiation

In this study, we consider the simplest and most classical approach to calculate discontinuity initiation, the so-called *strength hypotheses* [22]. According to this concept, a discontinuity may be initiated if the material is subjected to a determined stress condition above its plastic yielding. Therefore, we define a damage variable using the plastic deformation as  $D = \epsilon_p / \epsilon_{\text{limit}} \leq 1$ , where  $\epsilon_p$  is the plastic deformation, which depends on the yield criterion used and  $\epsilon_{\text{limit}}$  is a material parameter that defines the amount of plastic deformation before discontinuity initiation.

Then, we consider that the contact stress has a similar behavior as the internal stress with the exception that it does not produce traction forces. Therefore, any positive value of  $\tau_c$  in a principal direction is eliminated. To evolve the contact stress, we define an equivalent contact logarithmic strain as follows

$$\epsilon_c = \frac{1}{2} \ln \mathbf{B}_c; \quad \mathbf{B}_c^{\text{trial}} = \Delta \mathbf{F}_c \cdot \mathbf{B}_c^n \cdot \Delta \mathbf{F}_c; \quad \Delta \mathbf{F}_c = \mathbf{I} + \Delta t (\nabla \otimes \mathbf{v})^T. \quad (15)$$

Notice that, since the contact stress is calculated using the updated Lagrangian framework,  $\Delta \mathbf{F}_c$  must be calculated in the current configuration. The remaining of the return mapping is the same as explained in section 4.1. Since the contact stress refers to the reaction of the material under contact with an external body, we reset the logarithmic strain  $\epsilon_c$  of a particle  $i$  in the case that it is not in contact with any other particle. In other words, if there is not any neighboring particle  $j$  in which  $|\mathbf{r}_{ij}| < 1.5d$  and  $j \in \mathbb{U}_i$ , we set  $\epsilon_c = \mathbf{I}$  and, consequently,  $\tau_{c,i} = 0$ .

## 5 Numerical tests

### 5.1 Brazilian test

The Brazilian test is one of the most standard experiments to determine the tensile strength of a material. It consists of a cylindrical material sample placed sideways between two plates that exert a compressive force on the sample. Given a sample of radius  $R$  and length  $L$  without a hole, and considering that the sample detached at peak force  $P$ , the tensile strength of the material is given by  $\sigma_t = \frac{P}{\pi RL}$ , which considers that the material is brittle and its strength depends only on its tensile stress (that is, disregarding shear and compressive failures). Therefore, we have chosen a simple yield criterion that considers only the higher principal stress  $\sigma_1$  (or  $\tau_1$ ) to describe its plastic behavior. We follow the same material parameters as the physical experiment described in Li et al. [23] (elastic parameters are taken from Li et al. [24]) and fixed the values of  $d = 5 \times 10^{-4}$  m and  $\delta t = 10^{-8}$  s. To compare with Li et al. [23]'s results, we have simulated six models with different values of internal radius  $r$  for a hole placed in the center of the sample. To simulate a brittle fracture, we set the plastic deformation limit  $\epsilon_{\text{limit}}$  as 0.01 %. Gravity acceleration is ignored and the compressive plates are fixed with a velocity of 0.01 m/s.

Fig. 1 shows the resulting simulation for various values of  $r/R$  at the beginning ( $\varepsilon = 0$ ) and end of the simulation ( $\varepsilon = 0.1\%$ ). Qualitatively, the simulation was fairly successful, since it could reproduce the fact observed in Li et al. [23] that secondary horizontal cracks appears in samples with larger inner holes. The secondary cracks are also responsible for the appearance of a second peak in the evolution of  $P$  over time for samples with

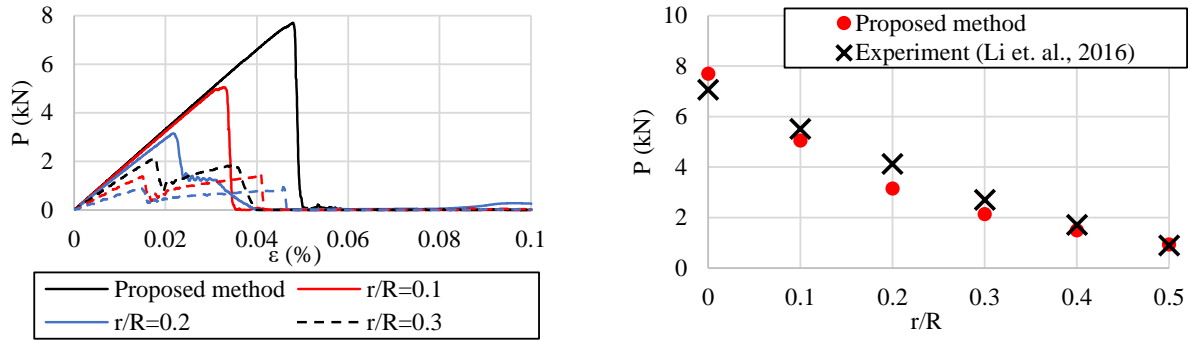


Figure 2. Brazilian test: graph of  $P$  over  $\varepsilon$  for different values of  $r/R$  (left) and graph of maximum  $P$  over  $r/R$  in comparison with experimental results [23] (right)

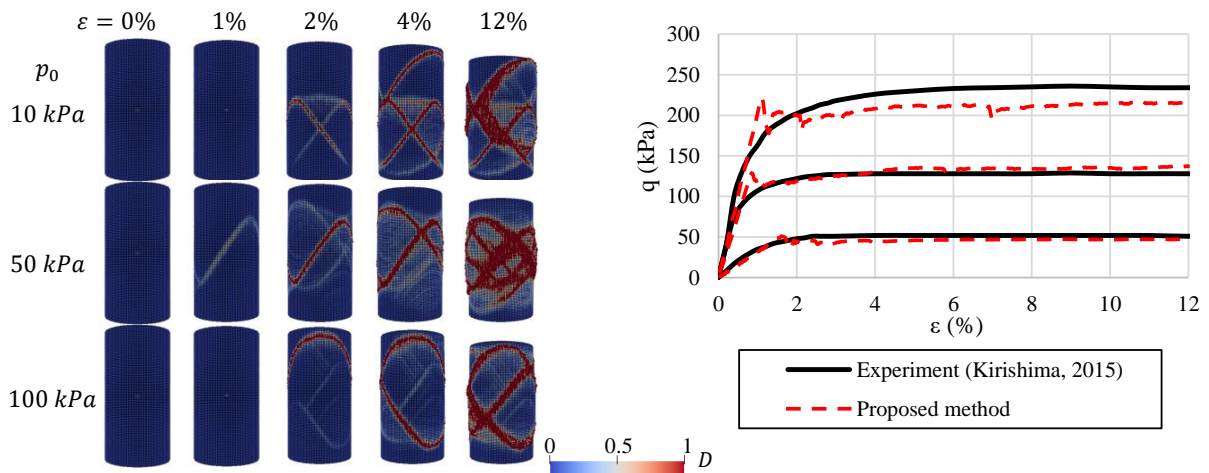


Figure 3. Triaxial compression test: snapshots of simulation results for different values of  $p_0$  and  $\varepsilon$  (left) and graph of  $q$  over  $\varepsilon$  for different values of  $p_0$  in comparison with experimental results [25] (right)

larger  $r/R$ , as shown in Fig. 2. Finally, we compare our results of maximum  $P$  for different values of  $r/R$  with the experimental results, showing a very good agreement between them. Including input/output of files, the computational performance was about 11 Mip/s (million iterations particles per second).

## 5.2 Triaxial compression test

This numerical example is the most important validation test, since our purpose with this study is to develop a numerical method for geomaterials in which the detached material keeps in contact with the original mass. In the triaxial compression test, the sample is loaded in all directions with a fixed water pressure  $p_0$ , and the side surface is protected by a rubber flexible material to avoid the water to infiltrate into the sample. To model this rubber material and the fixed pressure, we placed ghost particles around the sample that moves with the same velocity as the closest sample particle and fixed with a collision stress of  $\sigma_c = p_0 \mathbf{I}$ . The geometrical and material parameters are the same as Kirishima [25]. Gravity is neglected and the yield criterion is the Mohr–Coulomb with  $\varepsilon_{\text{limit}} = 0.1$ . Here we consider positive stress as compression in order to show the results in a familiar style for soil mechanics. In our numerical tests, we calculate the value of  $q$  as the force of the sample applied to the cap divided by the upper surface area minus  $p_0$ .  $d = 10^{-3}$  m and  $\delta t = 2/\text{times}10^{-6}$  s are fixed for all simulations.

Fig. 3 shows the simulation for different values of  $p_0$  and  $\varepsilon = h_c/H$ , where  $h_c$  is the displacement of the cap and  $H$  is the height of the sample initially. As expected, the resulting shear band follows an approximately  $50^\circ$  of inclination. The evolution of  $q$  also follows a similar pattern in comparison to the experimental results from Kirishima [25], as shown in Fig. 3. However, we observed a large peak value of  $q$  at the initiation of the plastic phase in our results, as well as some sudden drops in between. Such sudden drops reflect the initiation of a new discontinuity and the release of stress in the process. Since the scope of this work is to enable stable simulations of post-failure materials, we consider that this numerical test was successful. The computational performance was approximately 13 Mip/s including input/output of files.

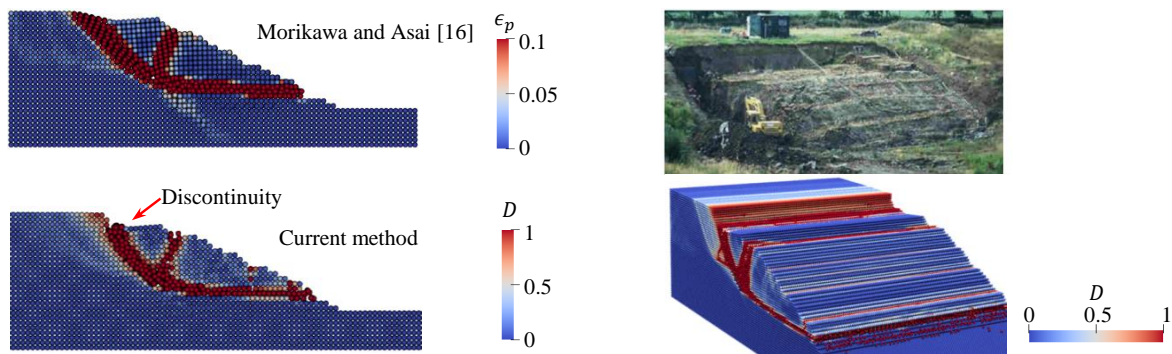


Figure 4. Selborne experiment: comparison of the simulation result at  $t = 50$  s between the proposed method and our previous results [14] ( $d = 0.5$  m) (left) and comparison between photo from Cooper et al. [26] and simulation at  $t = 50$  s in a 3D view (right)

### 5.3 Selborne experiment

The last numerical example is to show an application of the current method to a real world problem. Here, we consider the famous Selborne experiment [26], where a saturated soil slope of 1 : 2 is loaded with a water pressure at the bottom of the slope, so that a landslide is observed at the water pressure of  $p = 70$  kPa. To simulate the current problem, we included a soil-water coupling technique based on the  $\mathbf{u} - \mathbf{w} - p$  Biot's formulation in the same way as in Morikawa and Asai [14]. Please refer to this paper, if the reader is interested in understanding the details of the soil-water coupling formulation. The model geometry, boundary conditions, material parameters and others can also be seen in Morikawa and Asai [14].

Here, we show the capability of our method in reproducing clear discontinuities. Fig. 4(left) shows a snapshot of the simulation at  $t = 50$  s comparing our results with Morikawa and Asai [14] using the same particle diameter ( $d = 0.5$  m). In addition, we show a comparison between a photo from Cooper et al. [26] and our simulation in Fig. 4(right) (with  $d = 0.25$  m). From these two figures, it is clear that our current results are more realistic in the sense that it reproduces the actual phenomenon of the detachment of the soil mass during the landslide. Because of the solution of a pressure Poisson equation for the  $\mathbf{u} - \mathbf{w} - p$  formulation, the computational cost is lower compared to the previous numerical tests, being approximately 4 Mip/s

## 6 Conclusions

In this work, we have developed a mixed total Lagrangian–updated Lagrangian SPH method to simulate geomechanics problems with clear discontinuities. The core idea of the proposed method is to separate the internal forces within a body and the contact forces from the interaction with other bodies as an internal stress and a collision stress, respectively. Finally, to simulate discontinuities, we propose to use the plastic deformation as a measure of damage, so that fully damaged particles are detached from its previous body and are considered a separated particulate material (therefore, their interaction being calculated with the collision stress). Then, we validated the proposed method with the Brazilian test, triaxial compression test and the Selborne experiment. Computational time was acceptable, reaching 11 to 13 Mip/s for problems that does not involve water coupling and 4 Mip/s for problems with water coupling that requires solving a pressure Poisson equation.

We successfully accomplished the main goal of simulating the initiation of discontinuities and its following post failure behavior. In particular, we were able to reproduce the interaction between the detached material within a shear band and the intact material, showing a clear discontinuity between them. We are aware that the methods to model the initiation of discontinuities used in this work are generally simplistic, so usage of more elaborate methods such as phase-field may be a next target for future works.

**Acknowledgements.** This work was supported by the Japan Society for the Promotion of Science (JSPS) KAKENHI Grant Number JP-23KK0182, 23H01662 and 22H03601 and by SECOM Science and Technology Foundation. We also received computational environment support through the Joint Usage/Research Center for Interdisciplinary Large-scale Information Infrastructures (JHPCN) in Japan (Project ID: jh240032-NAH and jh230021-NAH).

**Authorship statement.** The authors hereby confirm that they are the sole liable persons responsible for the au-

thorship of this work, and that all material that has been herein included as part of the present paper is either the property (and authorship) of the authors, or has the permission of the owners to be included here.

## References

- [1] L. Lucy. A numerical approach to the testing of the fusion process. *Astron. J.*, vol. 82, pp. 1013–1024, 1977.
- [2] R. Gingold and J. Monaghan. Smoothed particle hydrodynamics: theory and application to non-spherical stars. *Astron. Soc.*, vol. 181, pp. 375–389, 1977.
- [3] J. Monaghan. Smoothed particle hydrodynamics. *Annu. Rev. Astron. Astrophys.*, vol. 30, pp. 543–574, 1992.
- [4] M. Asai, A. Aly, Y. Sonoda, and Y. Sakai. A stabilized incompressible sph method by relaxing the density invariance condition. *J. Appl. Math.*, vol. 2012, pp. 24 pages, 2012.
- [5] D. Morikawa, M. Asai, N. Idris, Y. Imoto, and M. Isshiki. Improvements in highly viscous fluid simulation using a fully implicit sph method. *Comput. Part. Mech.*, vol. 6, pp. 529–544, 2019.
- [6] D. S. Morikawa, K. Tsuji, and M. Asai. Corrected ale-isph with novel neumann boundary condition and density-based particle shifting technique. *Journal of Computational Physics: X*, vol. 17, pp. 100125, 2023.
- [7] A. Khayyer, H. Gotoh, H. Falahaty, and Y. Shimizu. An enhanced isph–sph coupled method for simulation of incompressible fluid–elastic structure interactions. *Comput. Phys. Commun.*, vol. 232, pp. 139–164, 2018.
- [8] D. Morikawa and M. Asai. Coupling total lagrangian sph-eisph for fluid-structure interaction with large deformed hyperelastic solid bodies. *Comput. Methods Appl. Mech. Engrg.*, vol. 381, 2021.
- [9] J. Bonet and T.-S. Lok. Variational and momentum preservation aspects of smoothed particle hydrodynamics formulations. *Comput. Methods Appl. Mech. Engrg.*, vol. 180, pp. 97–115, 1999.
- [10] C. H. Lee, A. J. Gil, G. Greto, S. Kulasegaram, and J. Bonet. A new jameson-schmidt-turkel smooth particle hydrodynamics algorithm for large strain explicit fast dynamics. *Comput. Methods Appl. Mech. Engrg.*, vol. 311, pp. 71–111, 2016.
- [11] C. H. Lee, A. J. Gil, A. Ghavamian, and J. Bonet. A total lagrangian upwind smooth particle hydrodynamics algorithm for large strain explicit solid dynamics. *Computer Methods in Applied Mechanics and Engineering*, vol. 344, pp. 209–250, 2019.
- [12] H. Bui, R. Fukagawa, K. Sako, and S. Ohno. Lagrangian meshfree particles method (sph) for large deformation and failure flows of geomaterial using elastic–plastic soil constitutive model. *Int. J. Numer. Anal. Methods Geomech.*, vol. 32, pp. 1537–1570, 2008.
- [13] T. Blanc and M. Pastor. A stabilized fractional step, runge–kutta taylor sph algorithm for coupled problems in geomechanics. *Comput. Methods Appl. Mech. Engrg.*, vol. 221–222, pp. 41–53, 2012.
- [14] D. Morikawa and M. Asai. Soil-water strong coupled isph based on u-w-p formulation for large deformation problems. *Comput. Geotech.*, vol. 142, 2022a.
- [15] D. S. Morikawa and M. Asai. A phase-change approach to landslide simulations: Coupling finite strain elastoplastic tispsh with non-newtonian iispsh. *Computers and Geotechnics*, vol. 148, pp. 104815, 2022b.
- [16] P. Randles and L. Libersky. Smoothed particle hydrodynamics: some recent improvements and applications. *Comput. Methods Appl. Mech. Engrg.*, vol. 139, pp. 375–408, 1996.
- [17] G. Ganzenmüller. An hourglass control algorithm for lagrangian smooth particle hydrodynamics. *Comput. Methods Appl. Mech. Engrg.*, vol. 286, pp. 87–106, 2015.
- [18] I. J. Schoenberg. Spline interpolation and best quadrature formulae. *Bull. Amer. Math. Soc.*, vol. 70, n. 1, pp. 143–148, 1964.
- [19] H. Hertz. Über die berührung fester elastischer körper (on the contact of elastic solids). *J. reine und angewandte Mathematik*, vol. 92, pp. 156–171, 1882.
- [20] K. Johnson. *Contact Mechanics*. Cambridge University Press, 1985.
- [21] de E. Souza Neto, D. Perić, and D. Owen. *Computational methods for plasticity: theory and applications*. John Wiley & Sons, Ltd, 2008.
- [22] D. Gross and T. Seelig. *Fracture Mechanics with an introduction to micromechanics*. Springer International Publishing AG, 2018.
- [23] D. Li, T. Wang, T. Cheng, and X. Sun. Static and dynamic tensile failure characteristics of rock based on splitting test of circular ring. *Transactions of Nonferrous Metals Society of China*, vol. 26, pp. 1912–1918, 2016.
- [24] X. Li, F. Feng, and D. Li. Numerical simulation of rock failure under static and dynamic loading by splitting test of circular ring. *Engineering Fracture Mechanics*, vol. 188, pp. 184–201, 2018.
- [25] T. Kirishima. Numerical simulation of geomaterials focusing on large deformation problems using the material point method (in japanese). *Shimizu Corporation research report.*, vol. Vol 92, 2015.
- [26] M. Cooper, E. Bromhead, D. Petley, and D. Grant. The selborne cutting stability experiment. *Geotechnique*, vol. 48, pp. 83–101, 1998.